Analysis of laboratory simulations of volcanic hybrid earthquakes using empirical Green's functions

Rebecca M. Harrington[1] and Philip M. Benson[2]

Received 18 March 2011; revised 28 June 2011; accepted 1 September 2011; published 9 November 2011.

[1] Here we present a new analysis of experimental simulations of the seismic signals characteristically observed in volcanic environments. We examine the waveforms of laboratory microseismic events generated during two rock deformation experiments performed on samples of Mt. Etna basalt to determine their source characteristics and establish evidence for a mode of failure. Events were recorded during deformation under (a), unsaturated (dry) conditions, and (b), samples saturated with water. We employ an empirical Green's function approach to isolate the acoustic emission event source spectra from attenuation and travel path effects, and estimate the spectral corner frequency using a least squares fit to a Brune spectral model. Spectral fits indicate that the acoustic emission events occurring under dry conditions follow the expected scaling of moment and corner frequency for standard brittle-failure in an elastic medium with constant stress drop, namely $M_0 \propto f_c^{-3}$. However, the events occurring during the fluid decompression phase of the saturated experiment have estimated corner frequencies which are not easily described by any simple scaling relationship. The implication of the observed scaling is that the events occurring under dry conditions must result from a standard stick-slip (i.e., brittle-failure) source. The observed moment-corner frequency scaling also suggests that event durations change in a predictable way with increasing moment for the events occurring under dry conditions. Conversely, events occurring under wet conditions do not show any distinctive relationship between duration and event size. The specific dependence of duration on event size exhibited by the events in the dry experiment must consequently rule out fluid-flow as a source, as there is no plausible reason for the driving pressure for fluid-flow to be dependent on duration in such a specific way. We compare laboratory observations of brittle-failure scaling ($M_0 \propto f_c^{-3}$) to previous observations of volcanic hybrid events in a field environment. Scaling dissimilarities between field observations and the wet laboratory events suggest that hybrid seismic signals observed in a volcanic environment do not always require fluid-flow to explain their signal.

Citation: Harrington, R. M., and P. M. Benson (2011), Analysis of laboratory simulations of volcanic hybrid earthquakes using empirical Green's functions, *J. Geophys. Res.*, *116*, B11303, doi:10.1029/2011JB008373.

1. Introduction

[2] Volcanic unrest is an ever present threat to nearby populations and economic interests on both land (e.g., agriculture), and in the air (e.g., air travel). Consequently, governmental agencies currently employ a diverse array of monitoring technologies to observe volcanoes, including ground deformation (GPS, tiltmeters), gas monitoring, and seismometers. The most important of these methods is arguably seismic signal analysis. The seismic signals observed in a volcanic environment are generally divided into classes based on frequency content [e.g., *Chouet*, 1996; *McNutt*, 2005]. Volcano-Tectonic earthquakes, and Low-Frequency earthquakes comprise two classes containing prominent pre-eruptive signals. Volcano-Tectonic (VT) earthquakes are indicative of faulting within the edifice; Low Frequency earthquakes (LF) are more commonly associated with fluids, and consist of two end-members: Long Period (LP) events, and volcanic hybrid events. LPs are generally acknowledged to be generated through resonance within buried structures (faults, cracks, and conduits) due to fluid movement [e.g., *Neuberg*, 2000; *Julian*, 1994]. Hybrid events exhibit features of both VTs and LPs. They typically commence with a high-frequency (VT-like) onset, transitioning to a low-frequency coda, similar to LPs. Complex models involving elastic failure, fluid oscillations, fluid shear, and the interactions between them are often invoked to explain both the high-frequency onset, and the low-frequency portion of the hybrid waveform [*White et al.*, 1998; *Neuberg et al.*, 2006; *Lahr et al.*, 1994]. Near-field

[1]Karlsruhe Institute of Technology, Geophysical Institute, Karlsruhe, Germany.
[2]Department of Earth Sciences, Geological Institute, ETH Zurich, Zurich, Switzerland.

0148-0227/11/2011JB008373

data (when it exists) has shown, in certain instances, that the long-period coda results from extended, volumetric source features [*Waite et al.*, 2008]. However, numerical work illustrates how the ambiguity of moment tensor inversions in a volcanic edifice is exacerbated by near surface structure and topography, calling into question the plausibility that volumetric or single-force focal mechanisms are as ubiquitous as they may seem [*Bean et al.*, 2008]. In other instances, observations suggest that for some low-frequency events much of the long-period coda results simply from the travel-path in the strongly attenuating volcanic edifice [*Harrington and Brodsky*, 2007; *Kedar et al.*, 1996; *Benson et al.*, 2010]. Understanding the role of fluids in the processes generating all the seismic signals observed in a volcanic environment is an important factor in understanding eruption dynamics, as the eruption style observed during volcanic unrest is often influenced by the presence of near-surface fluids [*Dingwell*, 1996; *McNutt*, 2005; *Saccorotti et al.*, 2007]. An increased understanding of how subsurface fluids are manifested in hybrid, and LP waveforms could improve the accuracy of forecasts, and may better facilitate our ability to anticipate eruptive style (e.g., effusive versus explosive).

[3] Although both VT and LP earthquakes are well studied [e.g., *Chouet*, 1996; *Neuberg et al.*, 2000, 2006; *Benson et al.*, 2007, 2008], the origins of hybrid type events are comparatively poorly known [e.g., *White et al.*, 1998; *Harrington and Brodsky*, 2007; *Kedar et al.*, 1996; *Iverson et al.*, 2006; *Lahr et al.*, 1994]. Understanding their origin is important, as the influence of pore fluids in their generation will likely provide greater insight into the processes occurring at depth. Although low-frequency seismic signals were previously thought to result exclusively from complicated interactions between elastic, solid, shear failure and fluid movement [*Julian*, 1994; *Chouet*, 1996], recent studies indicate that some LF signals may also result from simple shear failure [*McNutt*, 2005; *Tuffen et al.*, 2008; *Iverson et al.*, 2006; *Goto*, 1999; *Harrington and Brodsky*, 2007]. The lack of consensus on proposed hybrid sources results mainly from the difficulty in observing such seismic signals in the near-field, making the source mechanics difficult to infer [*Foulger et al.*, 2004; *Saccorotti et al.*, 2007]. A number of recent studies have concentrated on laboratory simulations of volcanic seismicity in order to obtain more detailed observations in a controlled environment.

[4] In order to address some of these challenges and better understand hybrid sources, we present a new analysis of experimental data simulating volcanic hybrid events collected by *Benson et al.* [2007]. The data sets consist of two rock deformation experiments performed on samples of Mt. Etna basalt under both water- (i.e., wet), and gas- (i.e., dry) saturated conditions. Both data sets were generated via standard (conventional) triaxial deformation experiments, with a suite of sensors arrayed around the test samples to detect Acoustic Emission (AE) events. AE event detection and analysis is a standard tool in rock deformation studies, as acoustic events recorded during rock deformation studies resemble earthquakes recorded on seismic networks in tectonic and volcanic settings [*Benson et al.*, 2008, 2010].

[5] The goal of the present work is to calculate and analyze source parameters of the AE events, such as seismic moment (M_0) and spectral corner frequency (f_c), in order to explore the changes in scaling between M_0 and f_c when water is present. Our observations show that M_0 and f_c scale according to brittle-failure scaling in the absence of water. We investigate how the laboratory M_0-f_c scaling relations compare with prior observations of scaling for hybrids observed in the field at Mount St. Helens. We discuss how the relative scaling similarities between the lab observations analyzed here, and the previous field observations suggest that some events observed in the field result from brittle-failure. We first provide a background and justification for using the empirical Green's function method to analyze source spectra of AE events recorded in the laboratory. Secondly, we show that the method is ideally suited for AE events, and tectonic events. Thirdly, we detail the data analysis procedures applied to obtain the source time functions of the laboratory events, and to estimate their M_0s and f_cs. By calculating the crack sizes implied by the estimated corner frequency values, we show that the similarity in observed crack sizes suggests the reliability of the method. Finally, we link our observations of AE event source parameter scaling to observations of volcanic hybrid source parameter scaling.

2. Methods and Observations

[6] Samples of basalt from Mt. Etna volcano (a porphyritic alkali lava-flow basalt of approximately 3.8% porosity and a density of 2860 $\frac{kg}{m^3}$) were deformed using a standard triaxial deformation apparatus installed at University College London (UK). Cylindrical samples 40 mm in diameter and 100 mm in length were isolated from a confining medium (silicone oil) via an engineered rubber jacket containing inserts for mounting piezoelectric sensors in order to detect AE events. AE events are an established and widely used tool in laboratory rock deformation studies, and are analogous to seismic signals at tectonic scales [*Benson et al.*, 2007; *Lockner et al.*, 2008; *Thompson et al.*, 2009]. AE event signals (voltages) are first pre-amplified 40 dB, before being received and digitized using a Vallen AMSY-5 AE event recorder at 10 MHz sampling rate. We tested two samples; a water saturated sample with a pore fluid (distilled water) pressure (P_p) of 20 MPa, and a dry sample using Nitrogen gas pressurized at 10 MPa. In both cases, a servo-controlled intensifier apparatus maintained an effective pressure ($P_{eff} = P_c - P_p$; where P_c is confining pressure) of 40 MPa. The ambient pressure conditions are broadly representative of the pressures expected at approximately 1.5 km depth within a volcanic edifice [*Benson et al.*, 2010]. The samples in both experiments were deformed at a constant axial strain rate of 5×10^{-6} s^{-1}, controlled via linear variable displacement transducers, producing a gradually increasing number of AE events up to sample failure. The AE events used in the analysis presented here consist of events occurring directly before failure, over a time span where velocity changes in the sample were negligible [*Benson et al.*, 2007]. The similarity of co-located event waveforms used in our analysis suggests that velocity changes are negligible. Therefore we use a single velocity value for the entire analysis. We discuss event similarity further in the methods description below.

[7] AE events are used here to explore the changing character of signals in volcano-tectonic regimes prior to

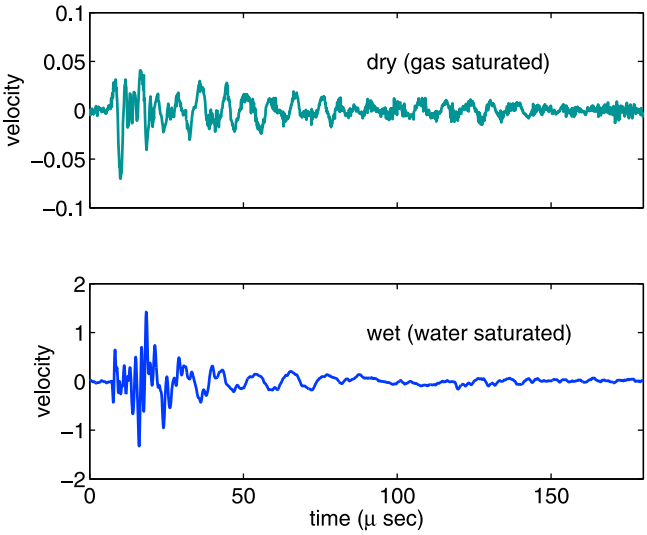

Figure 1. Example of AE event velocity waveforms recorded by piezoelectric (PZT) sensors during the (top) gas saturated (dry) and (bottom) water saturated rock (wet) deformation experiments performed on Mt. Etna basalt. Wave amplitudes units are calibrated according to the piezoelectric sensor, with unknown gain coefficient. Waveforms resemble volcanic hybrid earthquakes commonly observed preceding explosive volcanic eruptions with abrupt, high-frequency onsets, followed by lower-frequency ringing. (Estimated source duration of 0.5 μs suggests ringing lasts approximately 300 times longer, see text.)

eruption, by simulating the processes that occur under well constrained laboratory conditions. Specifically, we analyze the AE event signals during the two types of experiments using different pore fluids. Figure 1 depicts examples of AE event waveforms from both experiments. Both types of waveforms exhibit abrupt, high-frequency onsets in the first part of the waveform, followed by lower-frequency ringing in the later part of the waveform, two of the primary diagnostic features of volcanic hybrid events [*Neuberg et al.*, 2006; *Lahr et al.*, 1994; *Chouet et al.*, 1994]. The ringing in the example waveforms lasts approximately 300 times longer that the expected 0.5 μs source-durations, similar to hybrid events observed in the near field at Mount St. Helens [*Harrington and Brodsky*, 2007]. Source duration estimations are based on the average crack size observed in the hand samples following sample failure (~1 mm), and assuming a circular crack with a stress drop of 10 MPa. As introduced above, such events are sometimes observed at volcanoes capable of producing explosive eruptions, and are similar to recent swarms observed at Mount St. Helens, Redoubt, Montserrat, and Deception Island (see *Harrington and Brodsky*'s [2007] Figure 1 for comparison) [*White et al.*, 1998; *Lahr et al.*, 1994; *Iverson et al.*, 2006; *Neuberg et al.*, 2006].

[8] Although the AE event waveforms resemble those of volcanic hybrids observed in the field, their dominant frequencies are much higher than real hybrids. The frequency band of interest in the laboratory experiments ranges from 30 kHz to 1.2 MHz, determined by the range of the best signal-to-noise ratio. The data are filtered via hardware in the preamplifiers. In practice, we restrict ourselves to the range 250 kHz to 1.2 MHz, as the sensors are peaked at approximately 1 MHz, and have a flat response from 20 kHz [*Benson et al.*, 2010]. Such a frequency band is appropriate for the two experiments, as it permits observations of corner frequencies for crack sizes ranging from roughly 0.5–5 mm. Post-experiment examination of hand samples found microcrack sizes within this range (~1 mm).

[9] In order to infer the source characteristics from the spectral features of the AE events, we must isolate the source spectra from attenuation effects. When considering tectonic earthquakes, it is well-known that seismic attenuation is generally stronger in the high-frequency spectral band (above, for instance, 1–2 Hz). It is therefore likely that the high-frequency content of the AE events should be subject to strong attenuation effects, even over the short source-receiver distances within the rock sample [*Lundquist and Cormier*, 1980; *Hough et al.*, 1988; *Lekic et al.*, 2009]. Additionally, high-frequency attenuation effects are generally more pronounced in volcanic rocks that have been severely fractured and damaged[*Kedar et al.*, 1996; *Prejean and Ellsworth*, 2001; *Mayeda et al.*, 1991]. Failing to sufficiently account for the strong site and attenuation effects in volcanic rocks can lead to an underestimation of spectral corner frequency. An underestimation of corner frequency may, in turn, translate to an inaccurate estimation of the scaling between event size and duration [*Anderson*, 1986]. The high frequencies observed in the experiments conducted here on Etna basalt necessitate a thorough correction of attenuation effects in order to obtain an accurate estimation of corner frequency, and thus source duration. We therefore use an empirical Green's function (eGf) approach to recover the source time function (i.e., moment rate function) of the AE events. Such a method is ideal for isolating the source signal of a seismic event when a large number of events are clustered together spatially, as is the case in the rock sample shortly before failure [*Tuffen et al.*, 2008; *Benson et al.*, 2007, 2008].

[10] Specifically, our eGf method employs the spectral ratio between two events to recover the source spectrum of a single event. Theoretically, it resolves the source signal from all secondary effects, including, but not limited to, travel path effects, scattering, energy loss, site effects, and instrument response [*Hough and Dreger*, 1995; *Hough et al.*, 1991; *Nakanishi*, 1991]. The method requires that the two events have similar location, and thus similar waveforms, and differ by at least a unit of magnitude in size. If the above conditions are met, it is then possible to isolate the source spectrum of the larger event by dividing its spectrum by the smaller event's spectrum. The spectral division thereby cancels the non-source related effects such as those mentioned above.

[11] The method requires two assumptions: first, that signal distortion due to attenuation and propagation are linear over the magnitude range considered, and secondly, that the small event provides an eGf with a source displacement spectrum which is flat up to the corner frequency [*Hough et al.*, 1991; *Nakanishi*, 1991]. The resulting spectral ratio provides us with the source spectrum of the larger event scaled by the long-period portion of the smaller event spectrum. Using the eGf corrected spectra, one can obtain more accurate estimates of the spectral corner frequency than is possible using alternative methods that correct

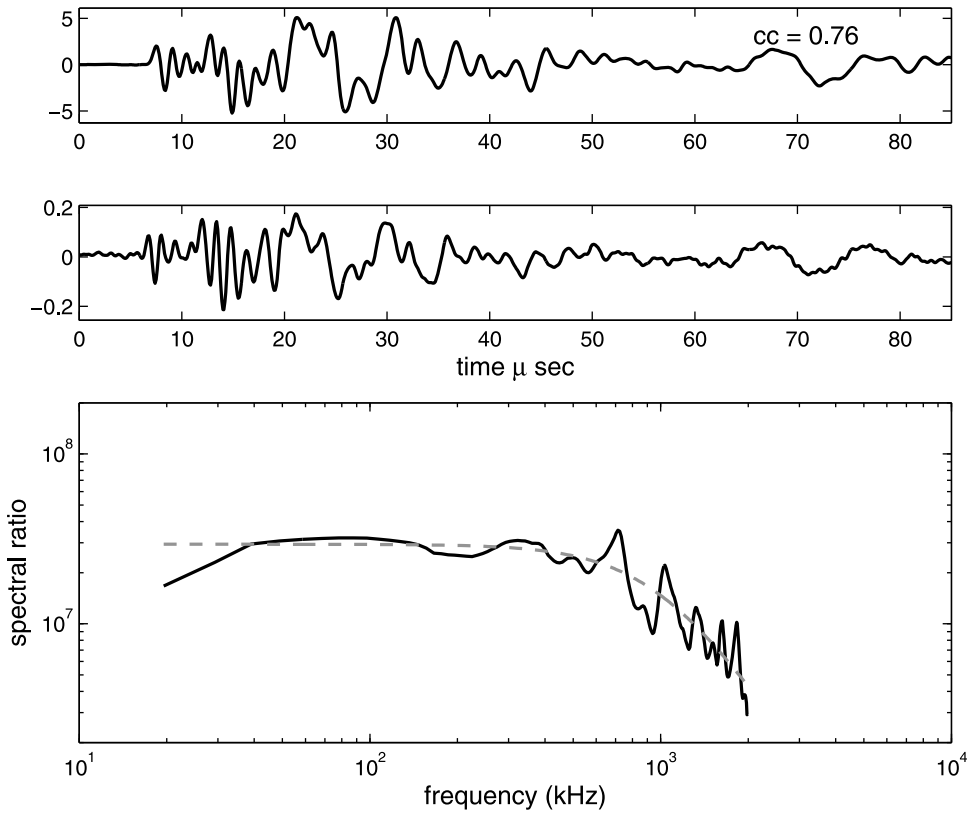

Figure 2. Event pair recorded on an individual sensor during the wet experiment. (top) Main event, (middle) empirical Green's function. The event pairs used for the empirical Green's function analysis must have at least a unit difference in magnitude, and a cross-correlation coefficient exceeding 0.65. The correlation coefficient for the event pair shown here is indicated in the top right corner of the top panel. The waveform similarity results from co-located sources, nearly identical travel paths, and the events being recorded on a common sensor. The spectrum of the smaller event is divided from the spectrum of the larger event, canceling all non-source related effects (e.g., site, travel-path attenuation, and instrument response) from the resulting source spectrum. (bottom). Resulting source spectrum (solid line) and Brune spectral model fit (dashed line).

spectral attenuation by estimating Q [*Abercrombie and Rice*, 2005; *Ide et al.*, 2003]. An advantage of the method is that no assumptions are required regarding the mode of failure. It is applicable to mode I failure, which might be expected in a rock deformation experiment with high fluid pressure, as well as modes II, and III shear failure. Crack expansion, hence rupture propagation, produces a similar, yet finite pulse, regardless of failure mode [*Anderson*, 2004; *Freund*, 1979]. A finite pulse produces a flat displacement spectra up to the corner frequency, which is ideally suited to such an analysis, provided the above size and location criteria are met.

[12] There are two potential problems associated with using the spectral ratio method on data obtained from rock deformation experiments. First, the unknown instrument response of the PZT sensors may cause a division by a small number, should there be a zero in the frequency band of interest. Such a problem is not unique to PZT sensors, and is a general concern for spectral ratio methods. To avoid spikes or holes in the source spectra, a water level is typically applied during the deconvolution process. We in fact had no need to apply a water level to the deconvolution, as examination of our source spectra indicated no such spikes indicative of division by a small number. Second, the velocity field changes as sample deformation progresses, as do the attenuation effects on the travel path from source to receiver. A large time difference between an eGf and a main event could change the signature of the non-source related spectral characteristics, causing them to no longer cancel. To address such concerns, we cross-correlate event waveforms, and impose a correlation-coefficient cutoff ($\geq$0.65) to insure waveform similarity, similar source-location/travel path, and therefore similar velocity field. In addition, changes in the relative velocity field should distort the resulting source spectra, producing a large model misfit. We impose a goodness of fit criteria (discussed in the next section) which removes source time functions that are poorly fit by a Brune spectral model, thereby removing events which may not be appropriate for the analysis method via quality control measures.

3. Estimating M_0 and f_c Values Using the Source Time Spectra

[13] As each experiment uses an array of 12 AE sensors, it follows that we record a maximum of 12 waveforms per

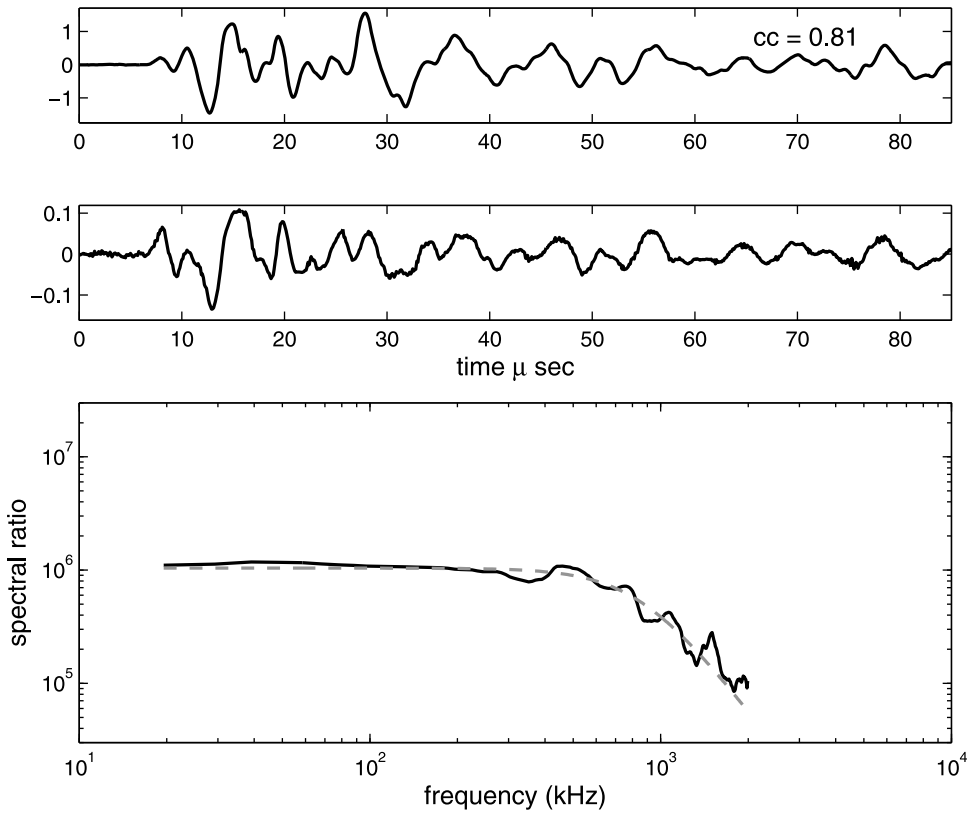

Figure 3. Event pair recorded on an individual sensor during the dry experiment. (top) Main event, (middle) empirical Green's function. The event pairs used for the empirical Green's function analysis must have at least a unit difference in magnitude, and a cross-correlation coefficient exceeding 0.65. The correlation coefficient for the event pair shown here is indicated in the top right corner of the top panel. The waveform similarity results from co-located sources, nearly identical travel paths, and the events being recorded on a common sensor. The spectrum of the smaller event is divided from the spectrum of the larger event, canceling all non-source related effects (e.g., site, travel-path attenuation, and instrument response) from the resulting source spectrum. (bottom) Resulting source spectrum (solid line) and Brune spectral model fit (dashed line).

event. In order to generate a high quality data set, we visually examine the AE event waveforms, discarding those which are clipped or for which no event is visually obvious above the noise level. The remaining data comprises the complete data set, consisting of 16,217 waveforms of 2177 AE events for the unsaturated experiment, and 6136 recordings of 640 events for the saturated experiment. Relative magnitude and location calculations are detailed by *Benson et al.* [2007], and are used here as well. The complete data analysis consists of a six-step procedure. We start by examining the AE event waveforms and cutting time windows of a specific length around each event. We remove events picked falsely by the automated picker, such as sporadic energy bursts. Next, we find suitable event pairs meeting the location and magnitude criteria using a grid search of event locations, based on locations and relative magnitudes determined by *Benson et al.* [2007]. We further sort suitable event pairs by imposing a minimum correlation coefficient criterion. We then calculate the channel-averaged source time spectra of the larger event in each of the pairs, imposing a more strict signal-to-noise cutoff than the waveform inspection performed in the first step. Next, we estimate the spectral corner frequency, and long-period spectral amplitude of the event source spectra using a least squares fit to a Brune spectral model. Finally, we estimate the model fit errors using a jackknife error estimation. We detail each of the data analysis steps below.

[14] We begin with the first step by cutting the waveform files with a window of 2048 samples, where each file begins 70 samples before the picked AE event arrival. Using 70 samples provides a large enough window so that a taper applied before Fourier transforming the time series does not affect the time series after the event arrival time. We do not make the assumption that the protracted ringing near the end of the waveform is simply coda (i.e., that all of the source information comes in the initial P- or S-wave arrivals), as such an assumption may be false for fluid related sources. We therefore use a time window which is long enough to include the entire waveform so as to capture any extended source signal which may exist.

[15] In the second step, we visually inspect the waveforms to make certain they are valid for the analysis. AE events were selected from the original recordings by an automated event detection method. An individual AE event is defined for each instance that a minimum of six sensors registers a voltage above a set threshold of 60 mV [*Benson et al.*,

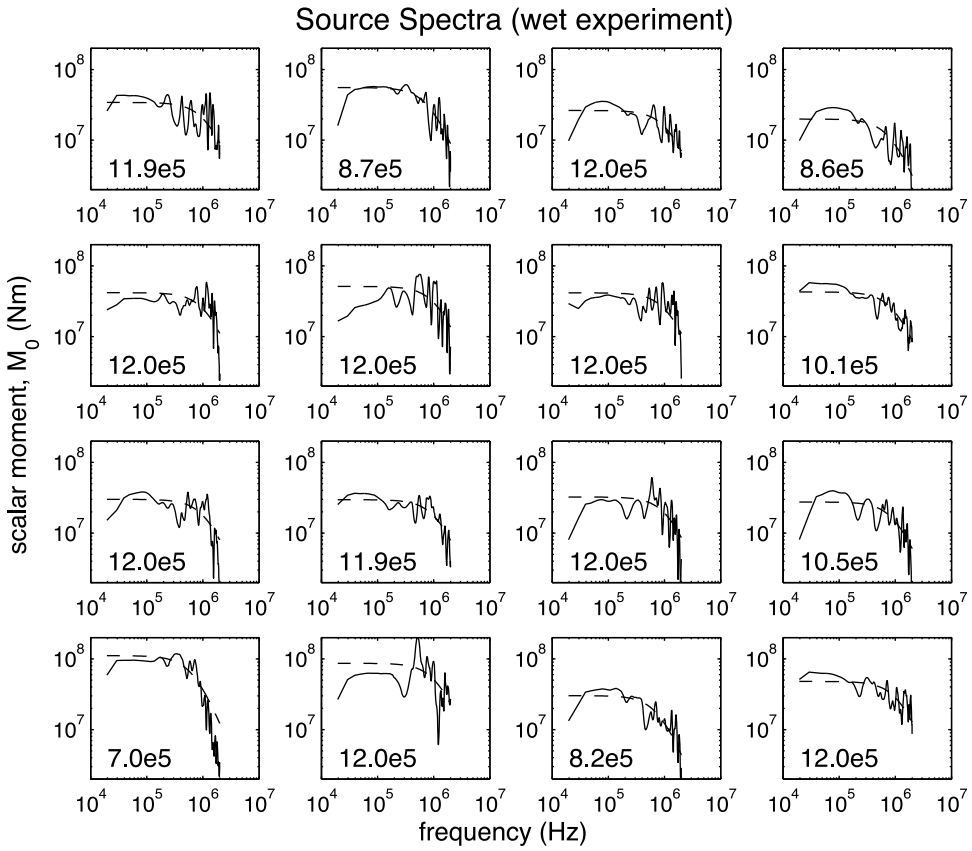

Figure 4. Source time function spectra (solid lines) for a set of events in the saturated experiment with sum of squared residuals value less than 10% of the sum of squared model values (see text). Dashed line represents the least squares fit to a Brune spectral model, with f_c value constrained to ≤1.2 MHz (the low-pass filter corner of the recording digitizer). Estimated corner frequencies shown in bottom, left corners. Note that many of the spectral corner frequency values are similar, suggesting little variation in source duration with event size.

2010]. We remove both clipped waveforms as well as a small number of events that resembled mechanical noise.

[16] In the third step, we perform a grid search of the event locations and magnitudes to find suitable event pairs for the eGf analysis. Individual event locations were determined using a downhill simplex routine and a triaxial velocity model to account for time dependent anisotropic seismic velocities resulting from crack formation and orientation dictated by the imposed stress field [*Benson et al.*, 2007, 2008]. Elastic wave velocity is measured by pulsing each of the sensors in turn, and measuring the resultant arrival on the remaining sensors to build up a 'pseudo' tomography of V_p. This is done periodically throughout the experiment to measure the V_p, and V_p anisotropy [*Benson et al.*, 2007]. *Benson et al.* [2008] estimate an average ±2 mm location accuracy.

[17] Event local magnitudes were determined via a path-weighted RMS voltage across the AE array following event location. It is important to note that laboratory AE (piezoelectric) sensors do not output calibrated acceleration or velocity data, in contrast to seismometers deployed in field settings. Relative seismic moments were calculated using the standard moment magnitude equation, employing the usual assumption for small events, namely, that the relative local magnitude is equal to the relative moment magnitude [*Hanks and Kanamori*, 1979]. Given that AE event magnitudes are determined by amplitude similarly to local magnitude (M_L), we use the $M_L = M_w$ equation to calculate relative moments. As mentioned in the previous section, the eGf approach requires having a pair of events with similar waveforms, and at least a unit of magnitude difference in size. We term the smaller event the eGf, and the larger event the "main event," as it is the event for which we determine the source time function by means of the spectral division. The similarity of waveforms between an AE event pair results from requiring all events to have both similar locations, which we ensure by imposing a minimum correlation coefficient criterion (Figures 2 and 3). (Counter to intuition, the AE event from the dry experiment in Figure 3 exhibits more low-frequency energy that the AE event from the wet experiment shown in Figure 2. However, such an observation does not generally hold for all events. We speculate that the event pair shown in Figure 3 may have occurred closer to sample failure, when damage is greater, and both seismic, and rupture velocities are slower).

[18] In addition to requiring waveform similarity via cross-correlation, we also require AE event locations to be separated by less than 5 mm. We create two $N \times N$ matrices **D** and **M**, where N is the number of events, each matrix entry D_{ij} represents the distance between event i and j

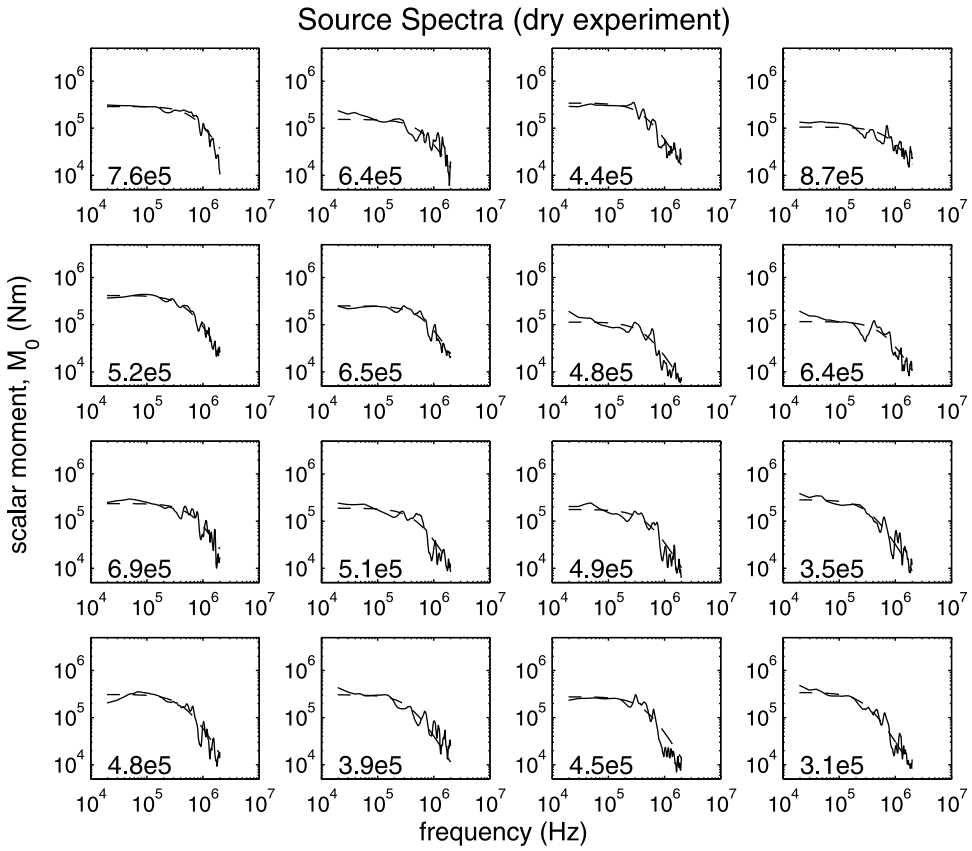

Figure 5. Source time function spectra (solid lines) for a set of events in the unsaturated experiment with sum of squared residuals value less than 5% of the sum of squared model values (see text). Dashed line represents the least squares fit to a Brune spectral model, with f_c value constrained to ≤1.2 MHz (the low-pass filter corner of the recording digitizer).

(meaning that the diagonal values must be zero), and each entry M_{ij} represents the magnitude difference between events i and j. We then choose event pairs with a distance less than 5 mm. Of those event pairs with distance ≤5 mm, we further restrict the set of viable pairs to those with a magnitude difference ≥1, and a cross-correlation coefficient ≥0.65.

[19] In the fourth step, we calculate the source time function spectra for the main events in each event pair. The source time function is defined as the spectral ratio between the channel-averaged main event and the eGf spectra. For each AE event, we first calculate the spectra on each individual channel and then multiply it by a scaling constant. The scaling constant is the reciprocal of the average of the first five data points corresponding to the flat portion of the source displacement spectra multiplied by the catalog magnitude. The absolute long-period displacement spectral amplitude of each channel recording is dependent on the source-receiver distance. Therefore, by multiplying by the scaling factor we ensure that the averaged spectra have a long-period amplitude which corresponds to the correct catalog moment, allowing us to later compare the scaling of other spectral features with AE event size (moment). The mean spectrum for each event consists of the mean of the individual scaled spectra. Channels with an average spectral amplitude signal-to-noise ratio less than five are removed from the mean spectral calculation. In principle, the eGf method can be used on a single station to obtain the source spectra of a given event. The advantage of using channel averages lies in the fact that it reduces any residual directivity or radiation pattern effects that may be present at the source, resulting from the case where events are not perfectly co-located. We therefore use the unique advantage of 3-dimensional azimuthal coverage that is not available for most source-receiver configurations, especially in field based data sets. The channel averaged spectra are used in the spectral division to calculate the source time function of each event, when multiple stations are available.

[20] In the fifth step, we calculate the seismic moment (M_0) and spectral corner frequency (f_c) for each of the source time spectra using a least squares fit to a Brune spectral model. Figures 4 and 5 show examples of the source time spectra and their spectral fits. We constrain the fitted f_c values to be less than 1.2 MHz, the low-pass corner applied to the preamplifiers. We consider only those events with a sum of squared residuals (SSR) which is less than 5% of the value of the sum of squared model (SSM) values for the dry experiment spectra. Applying the same criterion (i.e., SSR ≤ 0.05SSM) to the AE event spectra in the wet experiment leaves us with few data points. Therefore, we relax the goodness of fit criterion slightly to consider events with SSR ≤ 0.1SSM. Figure 6 illustrates the difficulty in fitting

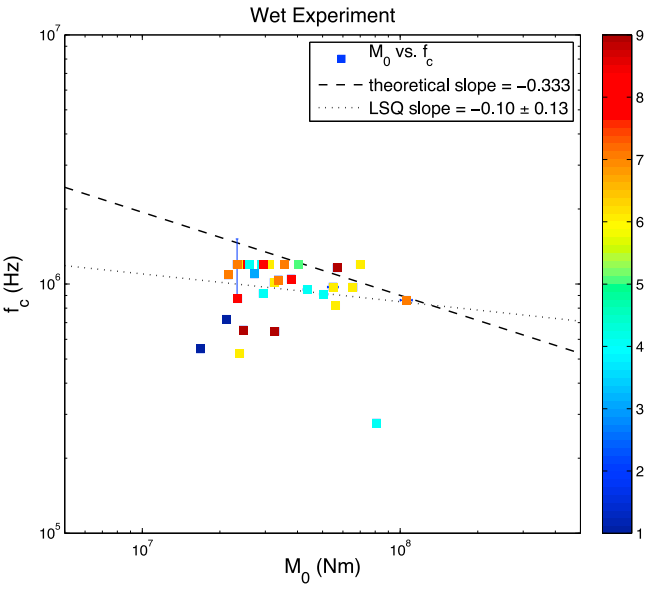

Figure 6. M_0 versus f_c values determined using a least squares fit to a Brune spectra for the source time spectra of the AE events in the water saturated experiment. Events shown have a sum of squared residuals value less than 10% of the sum of squared model values. Requiring the sum of squared residual values to be less than 5% (as in the case of the unsaturated experiment) leaves few data points. Error bars determined from the jackknife variance estimation (see text), and color coding indicates the number of channel recordings available for each AE event. The heavy dashed line indicates the theoretically expected slope for stick-slip ($M_0 \sim f_c^{-3}$). Short dashed line indicates the fitted slope with the confidence intervals of one standard deviation based on 10,000 bootstrap trials.

the spectra, as many of the estimated f_c values converge to the 1.2 MHz limit, suggesting that the Brune spectral model does not sufficiently describe many of the wet events. We speculate that the Brune model fits the spectra poorly, because the event durations do not change much with size. Events which do correspond well to the model have estimated corner frequency values that are consistent with observed crack sizes. We discuss the variation in duration and the consistency of crack sizes further in the last part of the discussion section.

[21] Finally, we estimate the error in the fitted M_0 and f_c values using a jackknife variance, similar to the method discussed by *Prieto et al.* [2007] for use with a single station. As many events have few stations which pass the rigorous correlation cutoff criteria, we use the single station estimation rather than a multiple-station error estimation as detailed by *Prieto et al.* [2007]. We take the average estimated error of the single station recordings for those events with multiple-channel recordings. Determining the jackknife variance consists of calculating each individual source spectrum using a multitaper algorithm which employs n Slepian tapers. To estimate the errors, the multitaper spectral calculation, as well as the M_0-f_c calculation is performed n-1 times, each time with one of the Slepian tapers removed. The procedure creates an $n-1$ group of M_0 and f_c values, from which the jackknife standard deviation values originate. These values are indicated in the error bars for the values estimated in both the saturated and unsaturated experiments in Figures 6 and 7. We then estimate the slope of the $\log(M_0) \propto \log(f_c)$ using the mean and standard deviation from 10,000 random replacement bootstrap trials. The confidence intervals for the estimated slope between $\log(M_0)$ and $\log(f_c)$ represents one standard deviation in residual values.

4. Discussion

[22] The eGf method produces event spectra for the dry experiment which resemble the displacement spectra of a standard earthquake, namely a flat spectral amplitude up to the corner frequency, with a f^{-2} falloff for higher frequencies (Figure 5) [*Haskell*, 1964; *Aki*, 1967; *Brune*, 1970]. Such spectra would result from the finite rupture of a mode I, II, or III crack in an elastic medium. The long-period spectral amplitude of such a source-duration pulse would be proportional to the size of the rupture (M_0), and would have a spectral corner frequency inversely proportional to the duration (τ, where $\tau \propto f_c^{-1}$). One can show using a mode II shear displacement how the size and duration (i.e., moment and corner frequency) would scale according to theoretical considerations as $M_0 \propto f_c^{-3}$ if stress drop is constant [*Kanamori and Rivera*, 2004; *Ide et al.*, 2003]. For example, a 2-D fault in an elastic medium has a scalar

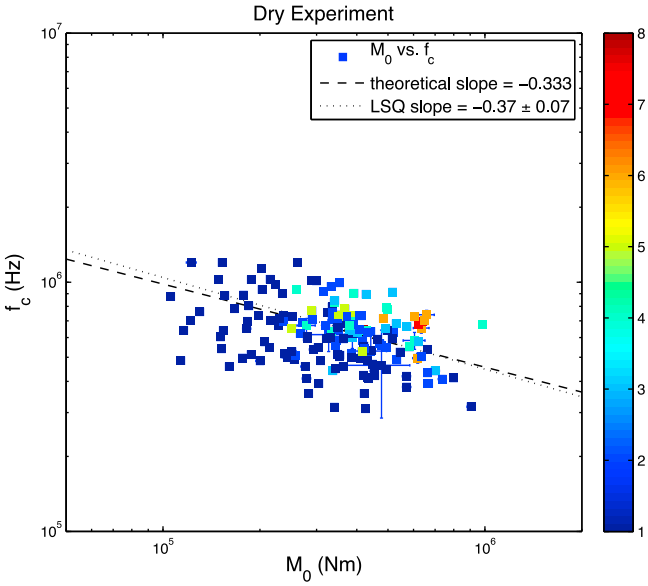

Figure 7. M_0 versus f_c values determined using a least squares fit to a Brune spectra for the source time spectra of the AE events in the unsaturated experiment. Events shown have a sum of squared residuals value less than 5% of the sum of squared model values. Error bars determined from the jackknife variance estimation (see text), and color coding indicates the number of channel recordings available for each AE event. The heavy dashed line indicates the theoretically expected slope for stick slip ($M_0 \sim f_c^{-3}$). Short dashed line indicates the fitted slope with confidence intervals of one standard deviation based on 10,000 bootstrap trials.

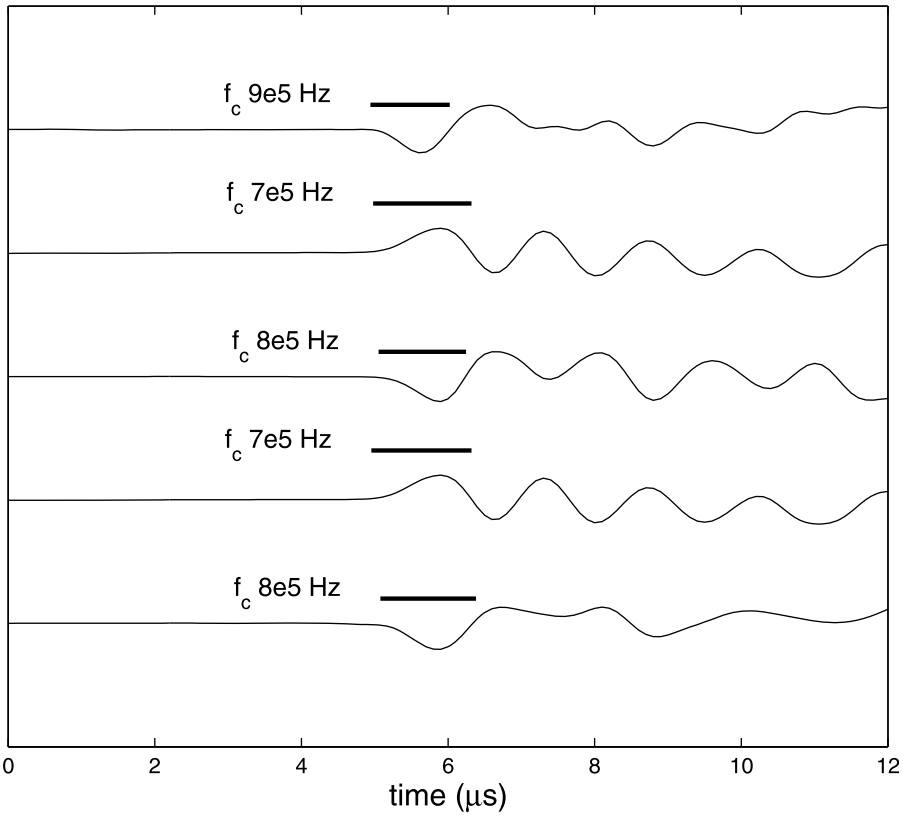

Figure 8. A representative sample of initial arrival pulses from the wet experiment suggests expected corner frequency values based on pulse width should be within the bandwidth of observation. Solid lines represent the width of the initial arrival, approximately representing source time function durations. Estimated f_c values are equal to the inverse of event durations (solid lines). The f_c values fall within the bandwidth of observation, suggesting many of the apparently flat spectra for the wet experiment may result from a small difference in AE event durations.

moment proportional to a series of double-couples, with moment given by [*Burridge and Knopoff*, 1964; *Keilis-Borok*, 1959]

$$M_0 = \mu A \bar{D}. \tag{1}$$

Considering that the static stress drop is proportional to the average fault slip divided by a fault length dimension, the equation for the moment of a circular fault can be written in terms of the stress drop and the fault radius

$$M_0 = \frac{16}{7}\Delta\sigma r^3, \tag{2}$$

where r is the fault radius, and $\Delta\sigma$ is the static stress drop [*Brune*, 1970, 1971]. We relate the source radius to the spectral corner frequency via

$$r = \frac{0.32}{f_c}\beta, \tag{3}$$

where β is the seismic shear velocity [*Madariaga*, 1976]. Substituting equation (3) into equation (2) provides the theoretically expected moment-corner frequency scaling for the case of elastic brittle-failure,

$$M_0 \propto f_c^{-3}. \tag{4}$$

[23] Based on the expected scaling for brittle-failure, one would expect that the M_0-f_c values estimated from the dry spectra should scale according to equation (4), if stress drops are constant. We note that in many rock deformation experiments, mode I failure may occur more predominantly than mode II failure. The scaling for other modes may differ from a mode II shear displacement depending on whether or not stress drop is constant. However, they should also scale in some consistent way. We do, in fact, observe the theoretically expected scaling for the dry experiment (Figure 7), suggesting that the stick-slip assumption is valid, regardless of the failure mode.

[24] Conversely, the spectra obtained from the eGf method for the wet experiment do not as closely resemble the expected displacement spectra of a Haskell-like source (Figure 4). Unlike the dry experiment event spectra, the corner frequency values are at times difficult to discern, with spectra that look flat over the frequency band of observation. In some cases, attempts to model the f_c values result in the optimization algorithm converging on the limiting f values determined by the upper corner of the band-pass filter applied to the data, implying that the apparent spectral corner may be a filtering effect rather than a source effect. Such an effect might suggest that the corner frequencies are outside our bandwidth of observation. However, corner frequency values that do not converge to filter values are

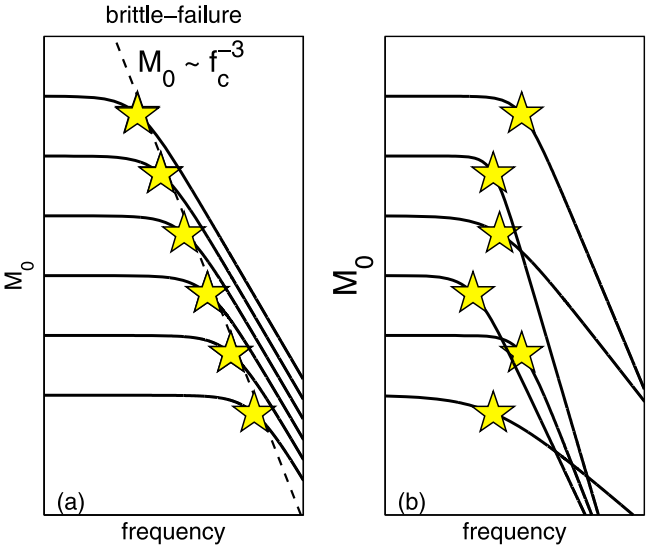

Figure 9. Schematic of the expected moment-corner frequency scaling for (a) brittle-failure, compared with (b) unknown moment-corner frequency scaling. Seismic events with a more complicated source involving some fluid component should deviate from the simple brittle-failure scaling, as fluid-flow may introduce a size (i.e. amplitude) dependence which varies from the simple case. As the only factor differing between the wet and dry deformation experiments is the presence of water, we infer that water must cause the observed deviation in scaling from the brittle-failure case in the wet experiment.

consistent with observed crack sizes in the rock sample. In addition, a sample of raw waveform pulses suggests that the pulse width of the initial arrival (which approximately represents the source time function) indicates that the expected corner frequencies are between the low- and high-frequency corners of the filter (Figure 8). Figure 8 shows a set of representative waveforms from the wet experiment, with solid lines indicating the width of the first arrival pulse, a proxy for the event duration. The estimated f_c values calculated from the inverse of the event duration lie within the bandwidth of observation. We speculate that the reason many of the wet event spectra look flat, is because there is little difference between the duration of the eGf and the main event (keeping in mind that Figures 4 and 5 are spectral ratios, not direct spectral observations). Such a hypothesis would be consistent with a small variation in f_c values. Many of the estimated f_c values for the wet experiment do, in fact, vary little with size, and do not indicate a predictable change in corner frequency with moment (Figure 6). We can not infer any specific details regarding the source processes of the AE events in the wet experiment based on the lack of simple moment-frequency scaling as seen in the dry experiment. However, it is precisely the deviation from brittle-failure scaling coupled with the known presence of water which suggests a failure mechanism other than simple stick-slip, elastic failure.

[25] Figure 9 schematically illustrates the scaling differences between elastic, brittle-failure and some general, alternative failure mode (e.g., an example alternative mode could involve some combination of brittle-failure and fluid-flow). In the case of brittle-failure, the moment and corner frequency values change in a predictable way relative to one another, as suggested by the theory presented in the beginning of the section. If scaling deviates from the brittle-failure case, it indicates that either the assumption of an elastic medium is false, or that the duration of the source, and thus the spectral corner frequency, is determined by some other mechanism than elastic, brittle-failure. An example of a mechanism which could change the size-duration relationship would be fluid-flow. A more complicated source resulting from non-elastic failure or fluid-flow would not have any such predictive scaling as indicated by the brittle-failure relationship in equation (4), requiring a deviation from the relationship. As illustrated in Figure 9b, the duration (f_c) may change more erratically with the size (i.e., the M_0), and the spectral falloff may also differ from the standard f^{-2} case predicted by common seismic source models [*Haskell*, 1964; *Brune*, 1970]. The schematic example in Figure 9b is just one example of how the $M_0 - f_c$ relationship may deviate from the relationship shown in Figure 9a due to a different source mechanism, but the key point is that it differs from the simple case shown in Figure 9a. For our particular data set, the temperature and the pressure conditions in the wet experiment are conducive to elastic, brittle-failure, making plastic/ductile failure unlikely. Furthermore, given that the presence of water is the only factor differing between the two experiments, we can infer that the presence of water is the cause of the observed change the size-duration scaling.

[26] Numerical models of LP events may provide insight into the lack of a discernible trend in size-duration scaling. *Julian* [1994] describes a model for long-period earthquake and tremor excitation in which a third-order, non-linear system of ordinary differential equations describe oscillations of the walls of an elastic conduit initiated by fluid-flow through the conduit. The amplitude of oscillations are dependent on the driving pressure difference between the ends of the conduit, with no correlation between amplitude and event duration. We suggest that the variations in spectral amplitude between different events during the wet experiment shown here may similarly correspond to different volumetric flow rates or pressure gradients through the conduit network in the basalt sample. The source duration may likewise be determined by fluid-flow driven by pressure gradients through a network of cracks.

[27] A comparison of the controlled conditions between the two experiments suggests that the observed $M_0 \propto f_c^{-3}$ scaling results from a standard stick-slip (i.e., brittle-failure) source. In the context of the laboratory observations presented here, we should be able to infer that if hybrid or other low-frequency earthquakes in a volcanic edifice do follow the brittle-failure scaling ($M_0 \propto f_c^{-3}$), then the mechanism of failure is simple stick-slip, and not the result of a fluid source. Conversely, a deviation from such scaling would suggest a mode of failure which may involve fluid-flow. In fact, observational evidence of volcanic hybrid earthquakes indicates that some hybrid signals may result from brittle-failure. *Harrington and Brodsky* [2007] perform a similar eGf analysis on the waveforms of a group of hybrid earthquakes associated with the 2004–2008 Mount St. Helens eruption, finding that the events follow brittle-failure scaling. The hybrid earthquakes were associated with the

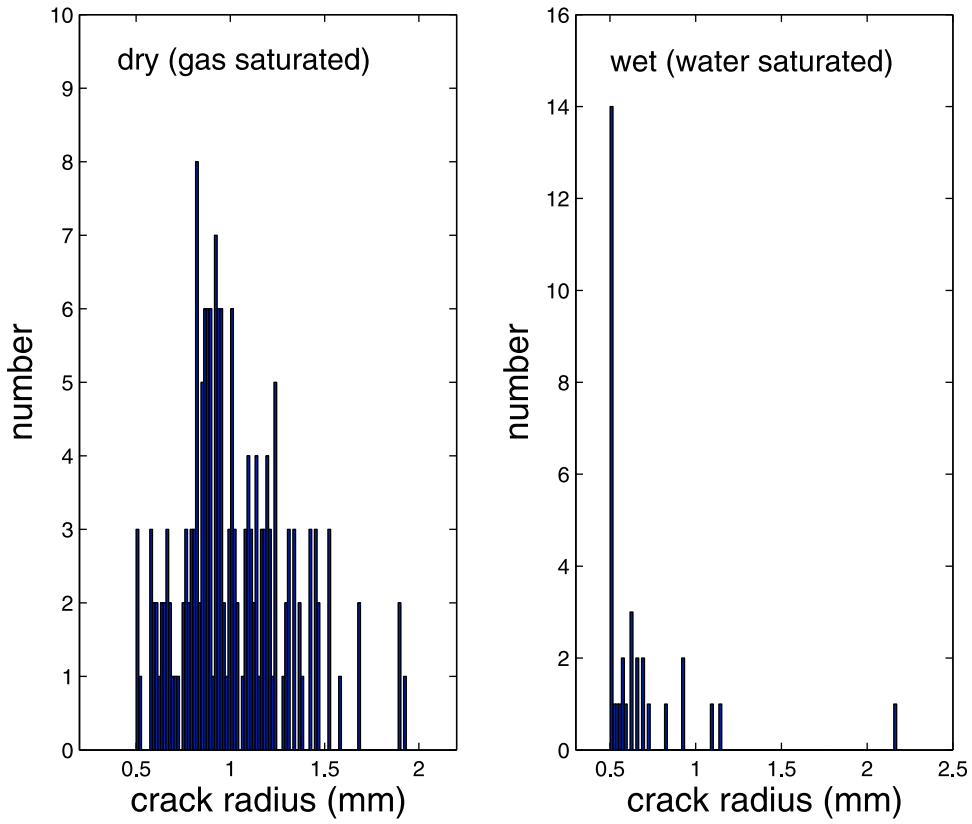

Figure 10. AE event crack radii values computed using equations (3) and (5), and modeled corner frequency values (Figures 6 and 7). Computed crack values range from 0.5 to 2.2 mm, and are consistent with ~1 mm crack radii observed in hand samples following the experiment. The consistency between computed and observed values suggests the reliability of the estimated corner frequency values.

extrusion of a number of solid rock spines in the crater, and were located primarily at the base of the actively extruding spines [*Moran et al.*, 2008; *Scott et al.*, 2008]. Extensive field and laboratory studies investigating the faulting environment and the rock properties of the extruding spine reveal the existence of typical shallow fault zone characteristics such as gouge, fault-surface striations, and fault zone cataclasite, all of which suggest stick-slip as a mechanism of failure [*Kennedy et al.*, 2009; *Cashman et al.*, 2008]. Based on the same reasoning used for the experimental events, one might be able to rule out fluid-flow as a source of a group of seismic signals if $M_0 \propto f_c^{-3}$ scaling applies, or establish the presence of if moment-corner frequency scaling deviates from the brittle-failure relationship.

5. Estimating Crack Size Using f_c Values

[28] The gain constants of the PZT sensors are poorly constrained, meaning that the seismic moment values measured are relative. However, one can estimate the crack radii of the AE events using corner frequency values in combination with a commonly accepted crack rupture model in an elastic medium. Here we use the estimated corner frequency values to calculate the crack radii.

[29] According to the plane circular model of an outwardly expanding crack given by *Madariaga* [1976], the compressional wave corner frequency and the crack radius (r) are related by equation (3). We use a value of β given by the seismic P wave velocity value and the relationship for a Poisson solid:

$$\beta = \frac{\alpha}{\sqrt{3}}. \tag{5}$$

Using equation (3), and a value of α = 3250 m/s for the Etna basalt produces crack radii values ranging from 0.5–2.2 mm (Figure 10). The majority of crack radii observed in the rock samples following the experiment were ~1 mm. We note that the range of crack sizes resulting from AE events is probably much larger than reflected in Figure 10. We examined a total of 640 and 2177 events in the wet and dry experiments respectively. Of those, only the 38 and 143 events shown in Figures 6 and 7, respectively, pass all of the necessary criteria described in the methods section, and can therefore be included in the analysis (i.e., magnitude difference greater than 1, signal-to-noise ratio, cross-correlation coefficient, and sum of squared residuals criteria). If we were able to use the eGf analysis on all of the events, we would surely observe a much larger range of crack-sizes. However, the strict criteria required to use the eGf method restrict the number of events which can be analyzed. (The same holds true for earthquakes in a tectonic setting). Nevertheless, the consistency of observed radii, and crack radii computed using the corner frequency values in the

subset of events suggests that the estimated corner frequencies are reliable.

6. Conclusions

[30] We obtain the source spectra of two groups of acoustic emissions events meant to simulate volcanic seismicity via deformation of Etna basalt under both wet and dry conditions. An estimation of the source characteristics using an empirical Green's function analysis suggests that the events occurring under dry or unsaturated conditions follow the expected scaling of moment and corner frequency for standard brittle-failure in an elastic medium with constant stress drop, namely, $M_0 \propto f_c^{-3}$. The spectra of the events in the dry experiment also resemble those of standard tectonic earthquakes. Spectra for events occurring under wet conditions are primarily flat, and many correspond poorly with a standard Brune spectral model. Their $M_0 - f_c$ scaling relationship shows that their spectral amplitudes do not scale in any particular way with their durations, suggesting that they are not the result of brittle-failure. Source scaling between the AE events in the wet experiment and the volcanic hybrids at Mount St. Helens differs, suggesting that the hybrids at Mount St. Helens do not occur as the result of a fluid process. Following such reasoning, similar scaling between the Mount St. Helens hybrids and the dry experiments suggests that the failure mechanism for the hybrid events must be similar to that in operation in the dry laboratory experiment. The observations imply that a $M_0 \propto f_c^{-3}$ scaling is characteristic general feature of elastic failure, and the presence of such scaling must exclude fluid-flow as a source of the seismic signal. Conversely, a deviation from the $M_0 \propto f_c^{-3}$ relationship may suggest a fluid induced seismic signal.

[31] **Acknowledgments.** We would like to thank Emily Brodsky and Ben Thompson for valuable comments which improved the quality of this manuscript. In addition, we would like to thank Chris Bean, Seth Moran, and one anonymous reviewer for their constructive suggestions. R. M. Harrington was supported by a fellowship from the Alexander von Humboldt Foundation, and P. M. Benson was partially supported by a Marie-Curie International Fellowship within the 6th European Community Framework program (contract MOIF-CT-2005-020167).

References

Abercrombie, R. E., and J. R. Rice (2005), Can observations of earthquake scaling constrain slip weakening?, *Geophys. J. Int.*, *162*, 406–424.

Aki, K. (1967), Scaling law of seismic spectrum, *J. Geophys. Res.*, *72*, 1217–1231.

Anderson, J. G. (1986), Implication of attenuation for studies of the earthquake source, in *Earthquake Source Mechanics*, *Geophys. Monogr. Ser.*, vol. 37, edited by S. Das, J. Boatwright, and C. H. Scholz, pp. 311–318, AGU, Washington, D. C.

Anderson, T. L. (2004), *Fracture Mechanics: Fundamentals and Applications*, 621 pp., CRC Press, Boca Raton, Fla.

Bean, C., I. Lokmer, and G. O'Brien (2008), Influence of near-surface volcanic structure on long-period siesmic signals and on moment tensor inversions: Simulated examples from Mount Etna, *J. Geophys. Res.*, *113*, B08308, doi:10.1029/2007JB005468.

Benson, P. M., B. D. Thompson, and P. G. Meredith (2007), Imaging slow failure in triaxially deformed Etna basald using 3D acoustic-emission location and X-ray computed tomography, *Geophys. Res. Lett.*, *34*, L03303, doi:10.1029/2006GL028721.

Benson, P. M., S. Vinciguerra, P. G. Meredith, and R. P. Young (2008), Laboratory simulation of volcano seismicity, *Science*, *322*, 249–252.

Benson, P. M., S. Vinciguerra, P. G. Meredith, and R. P. Young (2010), Spatio-temporal evolution of volcano seismicity: A laboratory study, *Earth Planet. Sci. Lett.*, *297*(1–2), 315–323.

Brune, J. N. (1970), Tectonic stress and the spectra of seismic shear waves from earthquakes, *J. Geophys. Res.*, *75*, 4997–5009.

Brune, J. N. (1971), Correction to "Tectonic stress and the spectra of seismic shear waves from earthquakes," *J. Geophys. Res.*, *76*, 5002.

Burridge, R., and L. Knopoff (1964), Body force equivalents for seismic dislocations, *Bull. Seismol. Soc. Am.*, *54*, 1875–1888.

Cashman, K. V., C. R. Thornber, and J. S. Pallister (2008), From dome to dust: Shallow crystallization and fragmentation of conduit magma during the 2004–2006 dome extrusion of Mount St. Helens, Washington, in *A Volcano Rekindled: The Renewed Eruption of Mount St. Helens, 2004–2006*, *U.S. Geol. Surv. Prof. Pap.*, *1750*, 1–29.

Chouet, B. A. (1996), Long-period volcano seismicity: Its source and use in eruption forecasting, *Nature*, *380*, 309–316.

Chouet, B. A., R. A. Page, C. D. Stephens, J. C. Lahr, and J. A. Power (1994), Precursory swarms of long-period events at Redoubt volcano (1989–1990), Alaska: Their origin and use as a forecasting tool, *J. Volcanol. Geotherm. Res.*, *62*, 95–135.

Dingwell, D. B. (1996), Volcanic dilemma: Flow or blow?, *Science*, *273*, 1054–1055.

Foulger, G. R., B. R. Julian, D. P. Hill, A. M. Pitt, P. E. Malin, and E. Shalev (2004), Non-double-couple microearthquakes at Long Valley caldera, California, provide evidence for hydraulic fracturing, *J. Volcanol. Geotherm. Res.*, *132*, 45–71.

Freund, L. B. (1979), The mechanics of dynamic shear crack propagation, *J. Geophys. Res.*, *84*, 2199–2209.

Goto, A. (1999), A new model for volcanic earthquake at Unzen volcano: Melt rupture model, *Geophys. Res. Lett.*, *26*, 2541–2544.

Hanks, T. C., and H. Kanamori (1979), Moment magnitude scale, *J. Geophys. Res.*, *84*, 2348–2350.

Harrington, R. M., and E. E. Brodsky (2007), Volcanic hybrid earthquakes that are brittle-failure events, *Geophys. Res. Lett.*, *34*, L06308, doi:10.1029/2006GL028714.

Haskell, N. A. (1964), Total energy and energy spectral density of elastic wave radiation from propagating faults, *Bull. Seismol. Soc. Am.*, *54*, 1181–1841.

Hough, S. E., and D. S. Dreger (1995), Source parameters of the 23 april 1992 M 6.1 Joshua Tree, California, earthquake and its aftershocks: Empirical Green's function analysis of GEOS and TERRAscope data, *Bull. Seismol. Soc. Am.*, *85*, 1576–1590.

Hough, S. E., J. G. Anderson, F. Brune, F. Vernon, J. Berger III, J. Fletcher, L. Haar, T. Hanks, and L. Baker (1988), Attenuation near Anza, California, *Bull. Seismol. Soc. Am.*, *78*, 672–691.

Hough, S. E., L. Seeber, A. Lerner-Lam, J. C. Armbruster, and H. Guo (1991), Empirical Green's function analysis of Loma Prieta aftershocks, *Bull. Seismol. Soc. Am.*, *81*, 1737–1753.

Ide, S., G. C. Beroza, S. G. Prejean, and W. L. Ellsworth (2003), Apparent break in earthquake scaling due to path and site effects on deep borehole recordings, *J. Geophys. Res.*, *108*(B5), 2271, doi:10.1029/2001JB001617.

Iverson, R. M., et al. (2006), Dynamics of seismogenic volcanic extrusion at Mount St. Helens in 2004–05, *Nature*, *444*, 439–443.

Julian, B. R. (1994), Volcanic tremor: Nonlinear excitation by fluid-flow, *J. Geophys. Res.*, *99*, 11,859–11,877.

Kanamori, H., and L. Rivera (2004), Static and dynamic scaling relations for earthquakes and their implications for rupture speed and stress drop, *Bull. Seismol. Soc. Am.*, *94*, 314–319.

Kedar, S., B. Sturtevant, and H. Kanamori (1996), The origin of harmonic tremor at Old Faithful geyser, *Nature*, *379*, 708–711.

Keilis-Borok, V. (1959), On estimation of the displacement in an earthquake source and of source dimensions, *Ann. Geofis.*, *12*, 205–214.

Kennedy, L. A., J. K. Russell, and E. Nelles (2009), Origins of Mount St. Helens cataclasites: Experimental insights, *Am. Mineral.*, *94*(7), 995–1004.

Lahr, J. C., B. A. Chouet, C. D. Stephens, J. A. Power, and R. A. Page (1994), Earthquake classification, location, and error analysis in a volcanic environment: Implications for the magmatic system of the 1989–1990 eruptions at Redoubt volcano, Alaska, *J. Volcanol. Geotherm. Res.*, *62*, 137–151.

Lekic, V., J. Matas, M. Panning, and B. Romanowicz (2009), Measurement and implications of frequency dependence of attenuation, *Earth Planet. Sci. Lett.*, *282*, 285–293.

Lockner, D. A., J. D. Byerlee, V. Kuksenko, A. Ponomarev, and A. Sidorin (2008), Quasi-static fault growth and shear fracture, *Nature*, *350*, 39–42.

Lundquist, G. M., and V. C. Cormier (1980), Constraints on the absorption band model of Q, *J. Geophys. Res.*, *85*, 5244–5256.

Madariaga, R. (1976), Dynamics of an expanding circular fault, *Bull. Seismol. Soc. Am.*, *66*, 639–666.

Mayeda, K., S. Koyanagi, and K. Aki (1991), Site amplification from S-wave coda in the Long Valley Caldera region, California, *Bull. Seismol. Soc. Am.*, *81*, 2194–2213.

McNutt, S. R. (2005), Volcanic seismology, *Annu. Rev. Earth Planet. Sci.*, *32*, 461–491.

Moran, S. C., S. D. Malone, A. I. Qamar, W. A. Thelen, A. K. Wright, and J. Caplan-Auerbach (2008), Seismicity associated with renewed dome building at Mount St. Helens, 2004–2005, in *A Volcano Rekindled: The Renewed Eruption of Mount St. Helens, 2004–2006*, *U.S. Geol. Surv. Prof. Pap.*, *1750*, 27–60.

Nakanishi, I. (1991), Source process of the 1989 Sanriku-oki earthquake, Japan: Source function determined using empirical Green-function, *J. Phys. Earth*, *39*, 661–667.

Neuberg, J. W. (2000), Characteristics and causes of shallow seismicity in andesite volcanoes, *Philos. Trans. R. Soc. Ser. A*, *358*, 1533–1546.

Neuberg, J., R. Luckett, B. Baptie, and K. Olsen (2000), Models of tremor and low-frequency earthquake swarms on Montserrat, *J. Volcanol. Geotherm. Res.*, *101*, 83–104.

Neuberg, J. W., H. Tuffen, L. Collier, D. Green, T. Powell, and D. Dingwell (2006), The trigger mechanism of low-frequency earthquakes on Montserrat, *J. Volcanol. Geotherm. Res.*, *153*, 37–50.

Prejean, S. G., and W. L. Ellsworth (2001), Observations of earthquake source parameters at 2 km depth in the Long Valley caldera, eastern California, *Bull. Seismol. Soc. Am.*, *91*, 165–177.

Prieto, G. A., D. J. Thomson, F. L. Vernon, P. M. Shearer, and R. L. Parker (2007), Confidence intervals for earthquake source parameters, *Geophys. J. Int.*, *168*, 1227–1234.

Saccorotti, G., I. Lokmer, C. J. Bean, G. Di Grazia, and D. Patane (2007), Analysis of sustained long-period activity at Etna Volcano, Italy, *J. Volcanol. Geotherm. Res.*, *160*, 340–354.

Scott, W. E., D. R. Sherrod, and C. A. Gardner (2008), Overview of the 2004 to 2006, and continuing, eruption of Mount St. Helens, Washington, in *A Volcano Rekindled: The Renewed Eruption of Mount St. Helens, 2004–2006*, *U.S. Geol. Surv. Prof. Pap.*, *1750*, 3–22.

Thompson, B. D., R. P. Young, and D. A. Lockner (2009), Premonitory acoustic emissions and stick-slip in natural and smooth-faulted Westerly granite, *J. Geophys. Res.*, *114*, B02205, doi:10.1029/2008JB005753.

Tuffen, H., R. Smith, and P. R. Sammonds (2008), Evidence for seismogenic fracture of silicic magma, *Nature*, *453*, 511–514.

Waite, G. P., B. A. Chouet, and P. B. Dawson (2008), Eruption dynamics at Mount St. Helens imaged from broadband seismic waveforms: Interaction of the shallow magmatic and hydrothermal systems, *J. Geophys. Res.*, *113*, B02305, doi:10.1029/2007JB005259.

White, R. A., A. D. Miller, L. Lynch, and J. Power (1998), Observations of hybrid seismic events at Soufriere Hills volcano, Montserrat: July 1995 to September 1996, *Geophys. Res. Lett.*, *25*, 3657–3660.

P. M. Benson, Department of Earth Sciences, Geological Institute, ETH Zurich, Sonneggstr. 5, CH-8092 Zurich, Switzerland. (philip.benson@erdw.ethz.ch)

R. M. Harrington, Karlsruhe Institute of Technology, Geophysical Institute, Geb. 6.42, Hertzstr. 16, D-76187 Karlsruhe, Germany. (rebecca.harrington@kit.edu)